# Structure-property relationship of defect-trapped Pt single-site electrocatalysts for the hydrogen evolution reaction

Peng Tang[1], Po-Yuan Huang[1], Jack E. N. Swallow[1], Chenbo Wang[2], Diego Gianolio[3], Hua Guo[1], Jamie H. Warner[4,5], Robert S. Weatherup[1], and Mauro Pasta*[1,2]

[1]Department of Materials, University of Oxford, Parks Road, Oxford OX1 3PH, United Kingdom
[2]Oxford Suzhou Centre for Advanced Research, 388 Ruoshui Road, Suzhou 215123, Jiangsu Province, P. R. China
[3]Materials Graduate Program, Texas Materials Institute, The University of Texas at Austin, 204 East Dean Keeton Street, Austin, Texas, 78712, United States
[4]Walker Department of Mechanical Engineering, The University of Texas at Austin, 204 East Dean Keeton Street, Austin, Texas, 78712, United States
[5]Diamond Light Source Ltd., Harwell Science and Innovation Campus, Chilton, Didcot, OX11 0DE, UK

## Experimental Section

### Chemicals

Chloroplatinic acid hexahydrate (37.5% Pt basis), aniline (99.5%), and ammonium persulfate (APS) (98%) were purchased from Sigma-Aldrich. Ultra-pure water (18.2 MΩ cm $^{-1}$; by Direct-Q Water Purification System) was used for the electrochemical tests.

### Catalysts synthesis

The Pt-PANI samples with varied Pt loading were synthesised by a wet impregnation method. Firstly, polyaniline was prepared via the oxidative polymerisation of aniline monomer with APS. [1] Then, the milled polyaniline was dispersed in ethanol solution and ultrasonicated for 30 mins; 10 mM $H_2PtCl_6$ dissolved in ethanol was transferred dropwise into the polyaniline solution under vigorous stirring for 4 h. Finally, the mixed solution was centrifuged at 10,000 rpm for 10 mins (repeated two or three times) to obtain the dry Pt-PANI powder after evaporating at 60 °C to remove the ethanol solvent. The trapped Pt SSC catalysts were prepared by pyrolysing Pt-PANI dry powder samples. Specifically, the Pt-PANI was placed in a tube furnace, and the temperature was increased from RT to 800 °C at a ramp rate of 15 min °C $^{-1}$. After reaching the setpoint temperature (800 °C), the Pt-PANI was annealed at 800 °C for 1.5 hrs to graphitise completely. The furnace was then left to cool naturally to obtain the final desired trapped catalysts.

### Ex-situ STEM and in-situ heating STEM

Room-temperature annular dark-field scanning transmission electron microscopy was performed with a JEOL ARM200F at an accelerating voltage of 200 kV. Dwell times of 10-20 µs, a beam current of 35 pA, and a

pixel size of 0.006 nm $px^{-1}$ were used for imaging, with a convergence semi-angle of 25.5 mrad and collecting inner-outer angles 68 to 275 mrad. The in-situ STEM experiments were performed at a lower accelerating voltage of 80 kV to minimise the beam damage to the system. An in-situ holder with a software-controlled heating chip developed by Dens solution company was used to deposit a 10 wt% Pt-PANI sample.

## Ex-situ XPS and temperature-dependent XPS

X-ray photoemission spectroscopy was performed using a PHI VersaProbe III system generating monochromatic Al X-rays at 1486 eV. A photoelectron take-off angle of 45◦ was used, and all measurements were performed at an X-ray power of 25 W and a chamber pressure less than 4E-9 mbar. Survey measurements were performed at a pass energy of 224 eV. In comparison, core levels were measured at a pass energy of 13 eV (26 eV), giving an energy resolution of 0.4 eV (0.45 eV) (determined from fitting a Fermi function convoluted with a Gaussian to the Fermi edge of a sputtered Au foil). The beam spot was circular with a nominal diameter of 100 µm. Samples were deposited directly onto gold foil for XPS measurements which negated the need for any charge compensation mechanisms.

For temperature-dependent XPS experiments, samples were transferred into a prep-chamber without breaking the vacuum to be heated (pressure in prep-chamber was 1E-8 mbar). Subsequently, samples were moved back into the XPS system through a load lock (pressure of 1E-6 mbar). In-situ heating was performed using a ceramic (pyrolytic graphite and boron nitride) heater from Thermic Edge, capable of reaching 1600 °C in UHV. A type K thermocouple was used to contact the Mo sample plate during heating to allow temperature measurements.

The binding energies were calibrated using the C 1s line at 284.8 eV in Figure 1 or Au 4f peak as references in Fig. 3i, j, k and Fig. 4c. The XPS spectra were fit using Gaussian-Lorentzian and Voigt lineshapes (where asymmetry was pronounced), and quantified with the help of CasaXPS software.

## Raman and FT-IR

The Raman spectra were collected with a Renishaw InVia microscope using a 532 nm laser. Multiple acquisitions were made with a 1% laser intensity for 1 s exposure time. The FT-IR spectra of the as-synthesized PANI, Pt-PANI, and Pt-PANI after pyrolysis were obtained using a Thermo Scientific Nicolet 6700 in transmission mode within a nitrogen-filled glovebox.

## Solid State Magic Angle Spinning NMR

All solid-state NMR experiments were performed on a 9.45 T Bruker Avance III HD NMR spectrometer, operating at $^{1}H$ and $^{15}N$ Larmor frequencies of 399.89 and 40.52 MHz respectively. A Bruker 4 mm double-resonance magic angle spinning (MAS) probe was used to facilitate a spinning frequency of 12 kHz. For the direct observation experiments, a 5.5 µs pulse and 100 kHz $^{1}H$ SPINAL-64 heteronuclear decoupling were utilised, whilst for the cross-polarisation experiments a 2.5 ms ramped (70-100 %) contact pulse was employed. A minimum of 2048 transients were recorded for each spectrum with a recycle delay of 3 seconds. The $^{15}N$ chemical shifts were referenced indirectly to neat liquid nitromethane ($CH_3NO_2$, 0 ppm) by using the secondary reference of powdered $^{15}N$ glycine (δiso = - 347.2 ppm). To convert to the chemical shift scale employed by protein NMR ($NH_3$ (l), -50 °C) it is necessary to add 379.5 ppm to the given shift.

## Electrochemical measurements

To drop-cast Pt powders on the glassy carbon electrode, 20 wt% commercial Pt/C (1 mg) or Pt SSC-based powder (4 mg) prepared by pyrolysis was mixed with ethanol (4 mL) and 5 wt% of Nafion (5 wt%, Sigma-Aldrich) and sonicated for at least 15 mins to obtain a homogeneous ink. The ink was then stirred at a rate of 500 rpm for 2 hrs to make a well-dispersed catalyst suspension. 20 µL of the suspension were dropped and coated on a glassy carbon electrode with an area of 1 $cm^2$ to achieve a catalyst loading of 1 $\mu g_{Pt} cm^{-2}$ on each sample. The catalytic activity of synthesised samples was evaluated using a three-electrode cell with

Pt metal mesh/graphite rod as counter electrode and $Hg/HgSO_4$ (in 0.5 M $H_2SO_4$) as reference electrode in 0.5 M pure $H_2$-purged $H_2SO_4$ solution. A 0.05 mm thick well-polished glassy carbon plate (Sigma-Aldrich Company Ltd.) was used to support the Pt powders. The GC supporting well-dispersed Pt catalysts with (1 $cm^2$) defined area were used as the working electrode. All the electrochemical tests were recorded by Biologic VMP3/SP240/SP150 potentiostats.

## Ex-situ and operando XAS

All X-ray absorption fine structure (XAFS) measurements at the Pt-$L_3$ edge were carried out at the B18 Core EXAFS beamline of the Diamond Light Source. For the ex-situ XAS, the Pt-PANI trapped Pt SSC, and Pt reference samples (300 mg) were finely ground, mixed homogeneously with five parts of cellulose, and pressed into 13 mm diameter pellets. Commercial dichloro[bis(pyridine)]platinum(II)($Pt(Py)_2Cl_2$, Sigma-Aldrich, 97%), $PtCl_2$ (Sigma-Aldrich, 99.995%) and PtTPP (Platinum(II) meso-tetraphenylporphine, Luminescence Technology Corp., >98%) were used as references. All spectra were recorded in transmission mode at room temperature.

The operando measurements were carried out using the Cr-coated branch of collimating and focusing mirrors, and a Si(111) double-crystal monochromator. The size of the beam at the sample position was ca. 1 mm × 1 mm. Samples were measured both in static electrolyte and operando conditions. The data were collected in fluorescence mode, by means of a 36-element solid-state germanium detector; the ion chamber at the front of the sample was used for measurement of incoming photons ($I_0$ filled with a mixture of 80 mbar of Ar and 1020 mbar of He to optimise sensitivity at 15% efficiency). An electrochemical cell adapted to the B18 beamline of the UK's Synchrotron Diamond Light Source was designed for the operando study shown in Supplementary Supplementary Fig. S19. Before the operando electrochemical measurements, the Pt-$L_3$ edge spectra were measured on contact with the liquid electrolyte. The operando XAFS spectra of the Pt-$L_3$ edge (11564 eV) were obtained from 200 eV before the edge up to 750 eV after the edge (corresponding to 14 $Å^{-1}$ in k-space). The measuring time was 2 minutes per spectrum. When indicated, 6 repetitions at each potential were acquired and then merged to obtain a better signal-to-noise ratio. Data were normalised using the Athena. [2] program with a linear pre-edge and polynomial post-edge background subtracted from the raw data. EXAFS fits were performed using ARTEMIS software. [2]

## Computational details

We used a plane-wave pseudopotential [3] density functional theory code (CASTEP v.21.11) for our simulations of trapped Pt SSC structures. [4] On-the-fly generated ultrasoft pseudopotentials were used to describe the ionic cores. A valance electron configuration of (4f14 5s2 5p6 5d9 6s1) with a core radius of 2.4 bohr was applied for Pt. 2s and 2p orbitals were treated as valance states for C and N with core radius of 1.4 and 1.1 bohr, respectively. A 520 eV energy cutoff, 20 % empty bands with a smearing of 0.1 eV and a k-point spacing of 0.04 Åwere used for all plane-wave calculations. The BFGS [5] line search was used for the geometry optimisation. The lattice constant $a$ for the single layer N-doped graphene model was obtained by geometry optimisation of the graphite structure using the Perdew-Burke-Ernzerhof (PBE) functional [6] with the many-body dispersion correction [7, 8] until the external stress and the force on each atom dropped below 0.05 GPa and $10^{-4}$ eV/atom. Grimme's D3 dispersion [9] correction was further adopted for optimising all geometries of N-doped graphene models. Three-layer (6×6) supercells of Pt-3N-C with 12 Å of vacuum slabs were used to investigate the hydrogen adsorption-free energy change on the surface of Pt-3N-C. The top two layers of the Pt-3N-C were allowed to optimise, while the third layer was fixed during the geometry optimisations. The hydrogen adsorption free energy ($\Delta G_{H^*}$) was calculated using the previously reported computational hydrogen electrode method by Nørskov et al. [10] with the following formalism:

$$\Delta G_{H^*} = \Delta E_H + \Delta ZPE - T\Delta S_H \quad (1)$$

where $\Delta E_H$ is the enthalpy change when one hydrogen atom is adsorbed on the N-doped graphene surface. $\Delta ZPE$ is the zero-point energy difference for the hydrogen adsorption with the $H_2$ value from Ref [11] at

298 K. $\Delta S_H$ accounts for the entropy contribution of the hydrogen adsorption at 298 K, which can be approximated as $-\frac{1}{2}S^0_{H_2}$ suggested by Noørskov et al., where $S^0_{H_2}$ is the entropy of hydrogen gas at standard conditions. [11, 12] For the hydrogen adsoprtion on the Pt site in the Pt-3N-C system, $\Delta E_H$ is obtained using Equation 2

$$\Delta E_H = \Delta E(H-Pt-3N-C) - E(Pt-3N-C) - \frac{1}{2}E(H_2). \quad (2)$$

$\Delta E(H-Pt-3N-C)$ is the DFT total energy of the hydrogen atom adsorbed Pt-3N-C slab, E(Pt-3N-C) is the total energy of the pristine Pt-3N-C surface and $E(H_2)$ is the DFT-calculated total energy of the hydrogen gas. The same formulism is used for the calculation of $\Delta G_{H^*}$ on N site and C site in 3N-C system. $\Delta E_H$, ZPE and entropy corrections for the Pt(111) surface and the Pt-3N-C/3N-C models are listed in table S1. The hydrogen adsorption energy of the Pt(111) surface is calculated using 25 % of hydrogen coverage on a three layer Pt(111) slab with the top two layers allowed to relax in a 2 × 2 unit cell. Schematic drawings for Pt-3N-1C were produced using VESTA v.3. [13]

**Table S1:** Summary of hydrogen adsorption energy calculations.

| Models | $\Delta E_H$ | $\Delta ZPE - T\Delta S_H$ |
|---|---|---|
| Pt site (Pt-3N-1C) | 0.37 | 0.25 |
| N site (3N-1C) | -1.66 | 0.36 |
| C site (3N-1C) | -2.87 | 0.32 |
| Pt(111) | -0.56 | 0.26 |

# Additional results and discussion

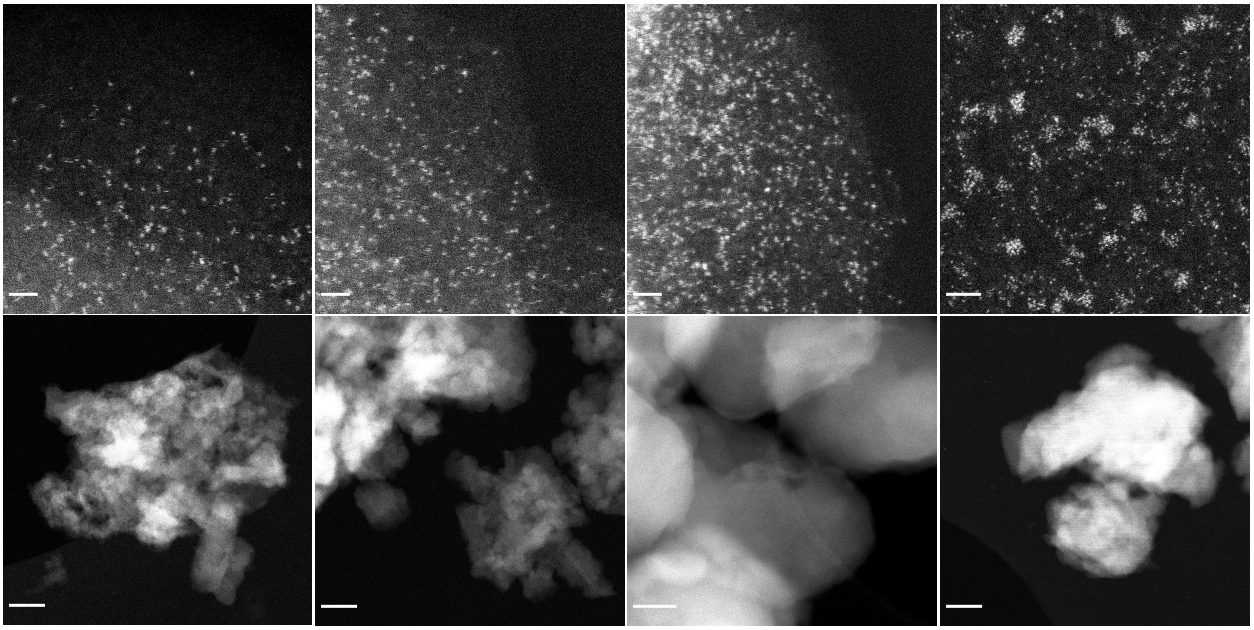

**Figure S1:** Atomic-resolution HAADF-STEM images show the edge positions of the 2 wt% (**a**), 5 wt% (**b**), 10 wt% (**c**), and 15 wt% (**d**) Pt-PANI samples. Low-resolution STEM images of the 2 wt% (**e**), 5 wt% (**f**), 10 wt% (**g**), and 15 wt% (**h**) Pt-PANI samples present the lack of nanoparticles over large areas of those samples. The scale bar is 2 nm in **a**-**d** and 100 nm in **c**-**f**).

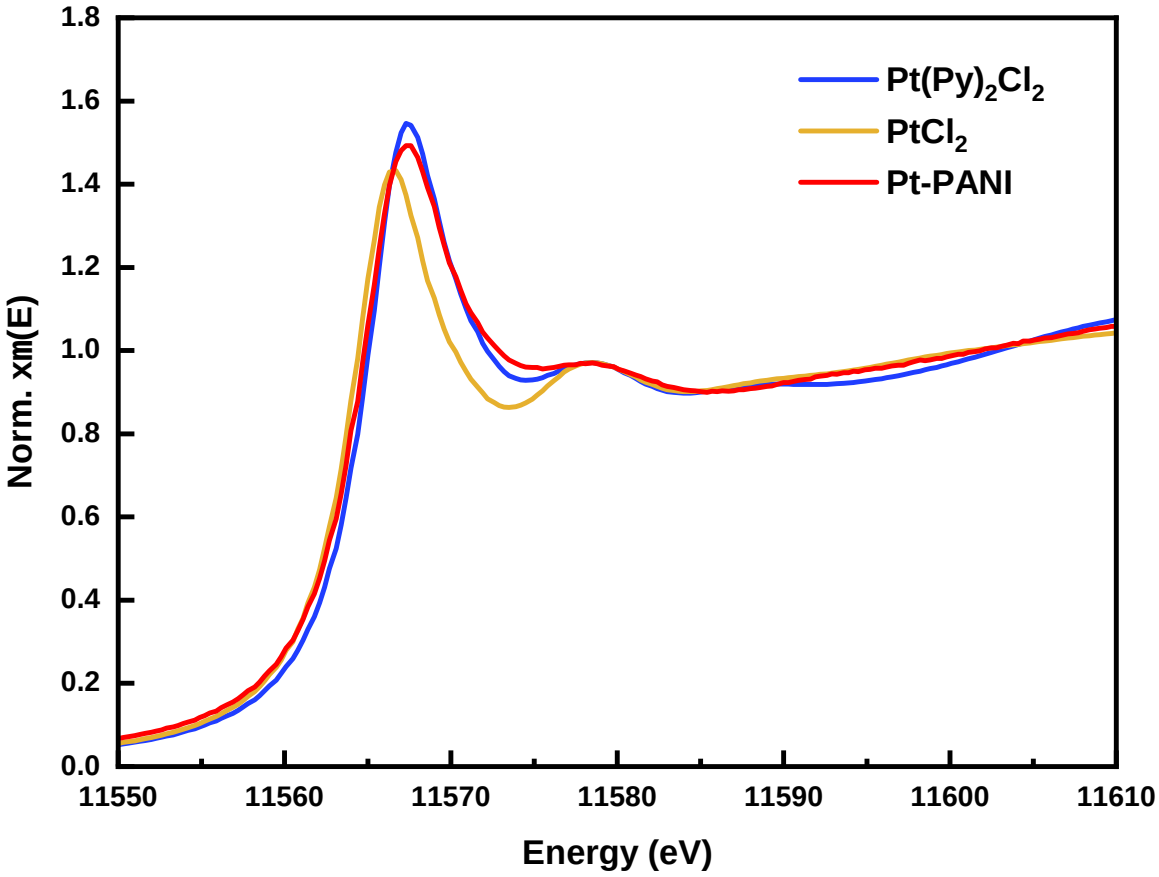


**Figure S2:** XANES of the Pt-PANI sample, compared with $Pt(Py)_2Cl_2$ and PtCl2.

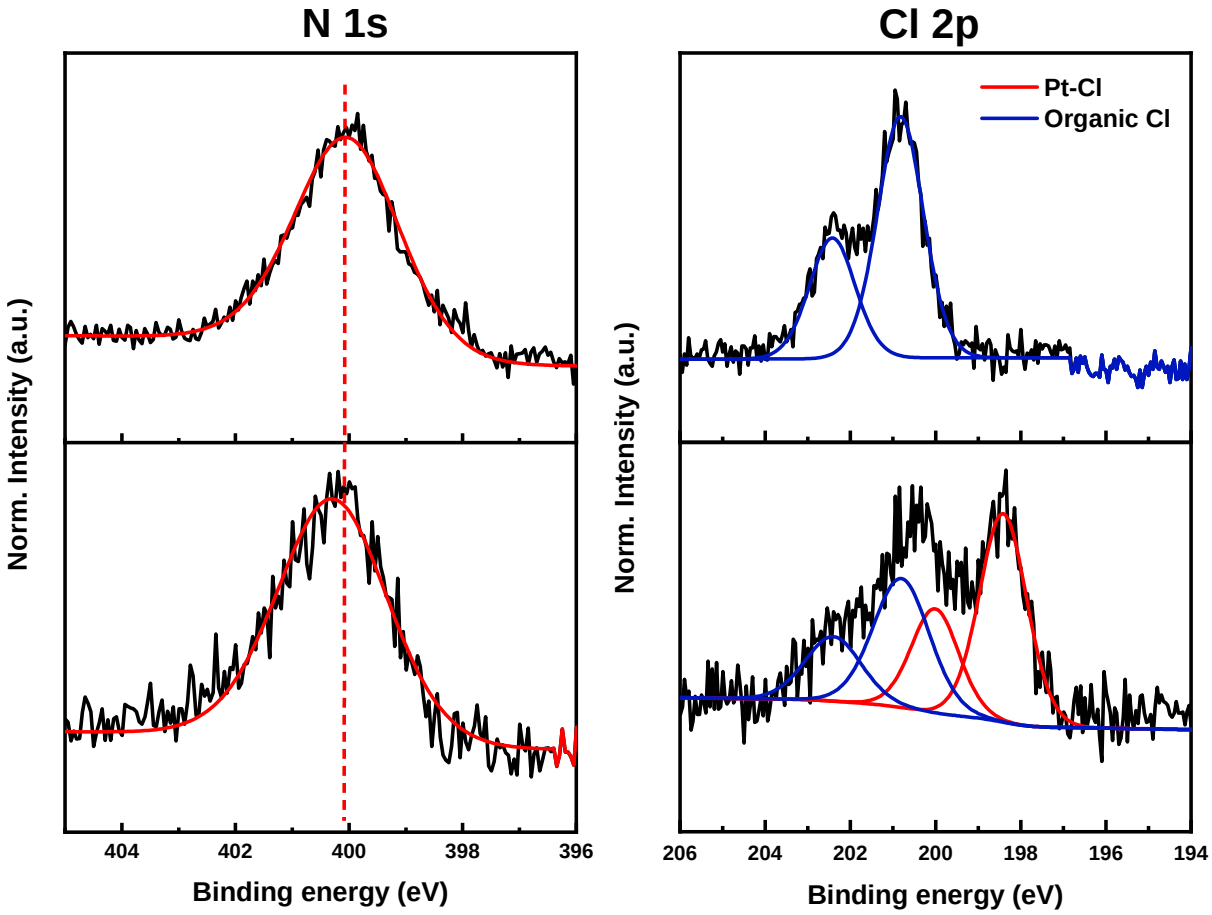


**Figure S3:** XPS spectra of N 1s and Cl 2p of the PANI and 10 wt% Pt-PANI samples.

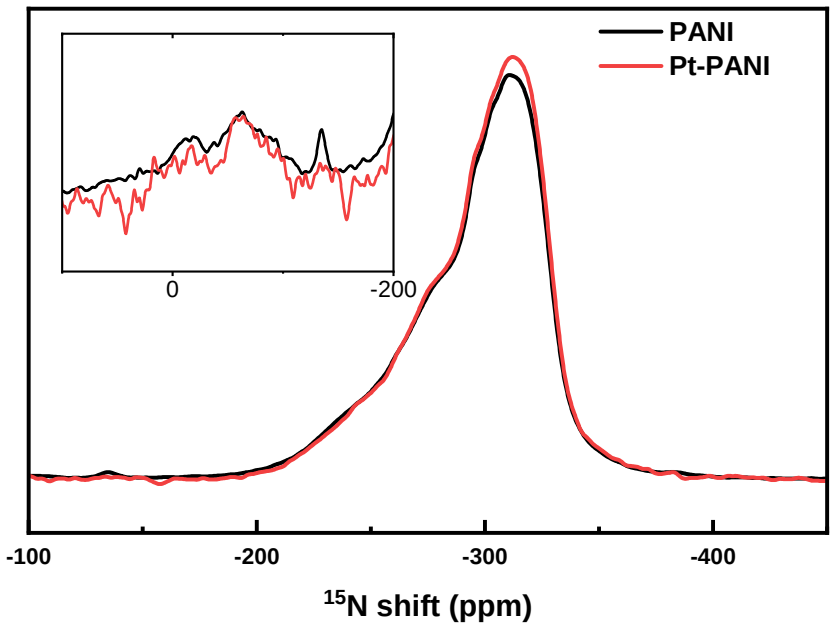


**Figure S4:** $^{15}$N CPMAS NMR spectra of the PANI and 10 wt% Pt-PANI samples showing a slight shift of the peak after anchoring of Pt sites.

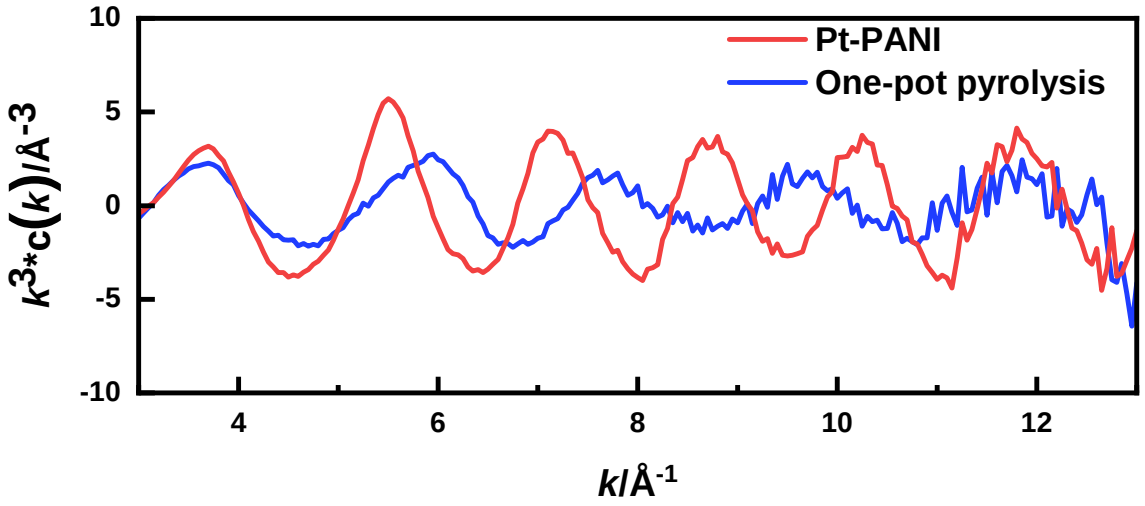


**Figure S5:** FT-EXAFS of 1 wt% Pt-PANI in K-space before and after pyrolysis, which clearly shows the changes in the bonding environment of Pt

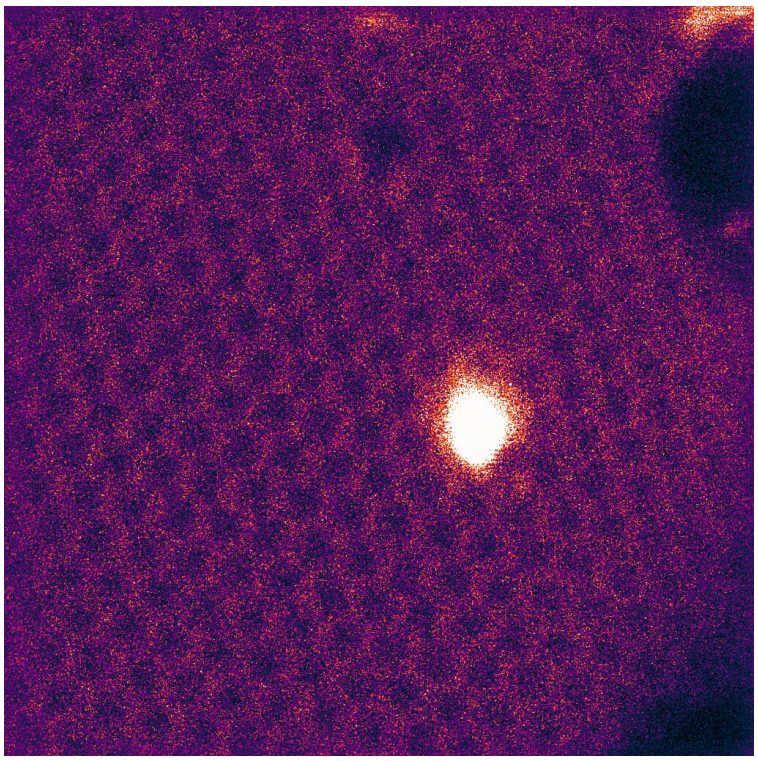

**Figure S6:** Atomic Z-contrast HAADF-STEM image of a Pt site supported at the surface of a defective single-layer graphene nanosheet, providing direct evidence that the use of STEM imaging to confirm the bonding between Pt sites and a graphene substrate is technically challenging due to the high contrast difference between C or N and Pt.

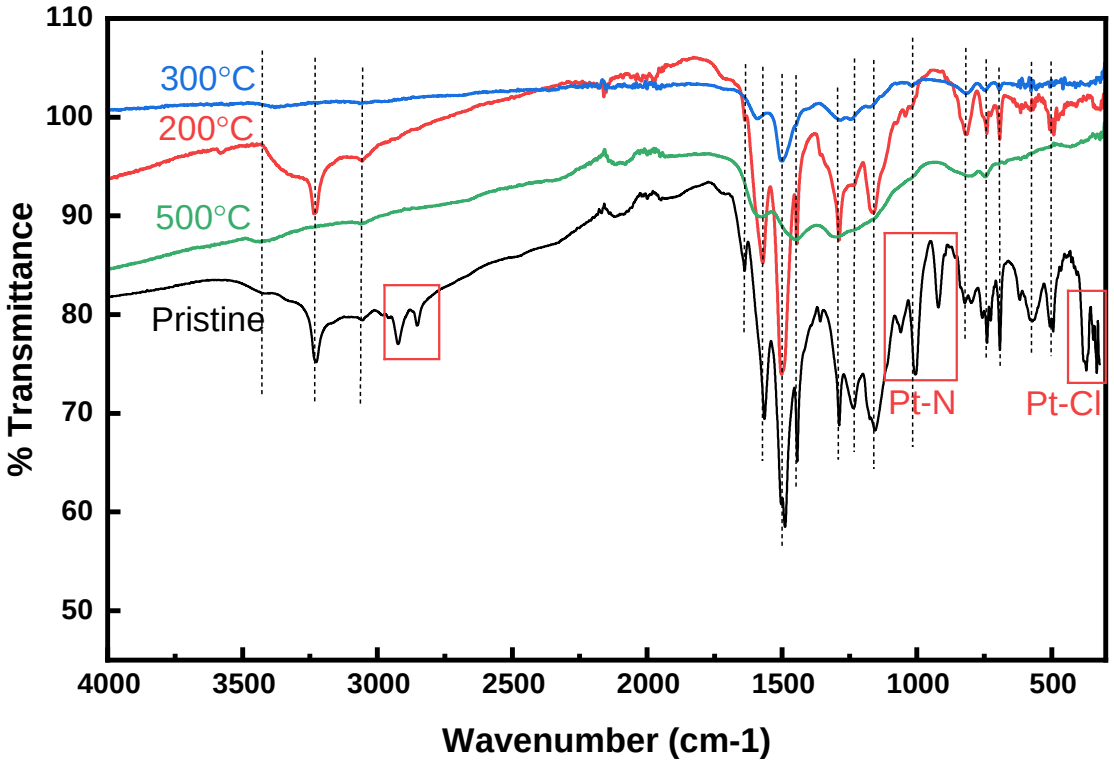


**Figure S7:** Ex-situ FT-IR spectra of the 10 wt% Pt-PANI sample after heating at different temperatures, showing the evolution of the PANI substrate and Pt bonding environment

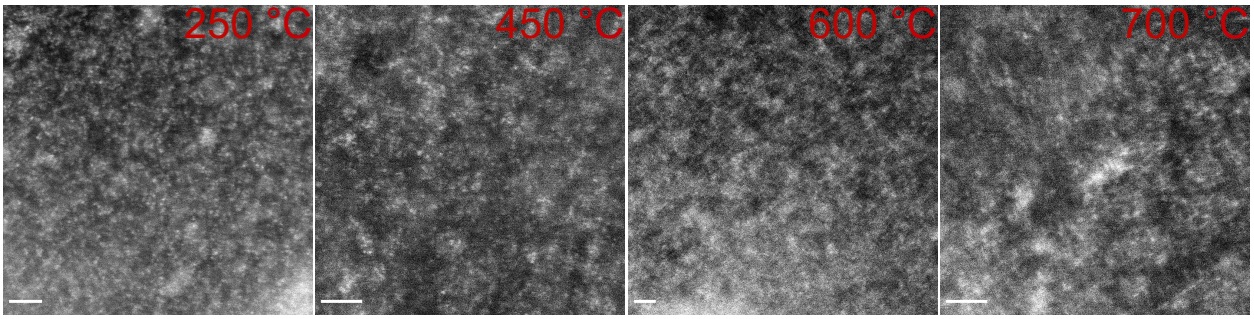


**Figure S8:** In-situ heating STEM images of Pt sites at the bulk areas (**a-d**) in the 10 wt% Pt-PANI sample at more heating temperatures (250 °C, 450 °C, 600 °C, and 700 °C). The scale bar is 2 nm in **a-d**.

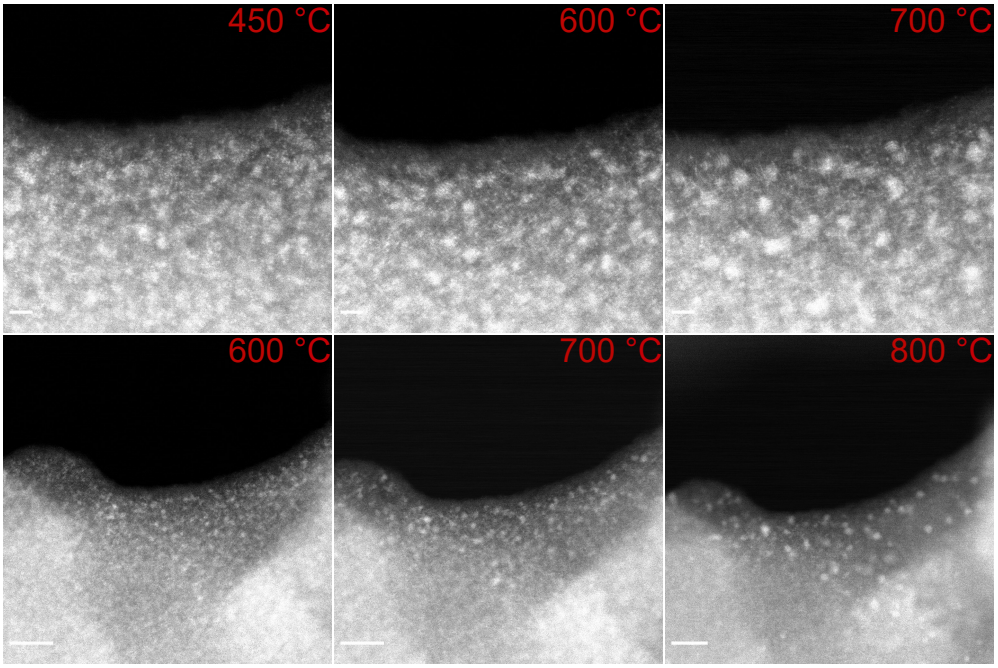


**Figure S9:** **a-c**, High-resolution in-situ heating STEM images of Pt sites at the edge areas in the 10 wt% Pt-PANI sample at more heating temperatures (450 °C, 600 °C, and 700 °C). The scale bar is 2 nm in **a-c**. **d-f**, Zoomed-out STEM images of Pt sites at the edge areas in the 10 wt% Pt-PANI sample at more heating temperatures (600 °C, 700 °C, and 800 °C), which show the formation of Pt nanoparticles. The scale bar is 10 nm in **d-f**.

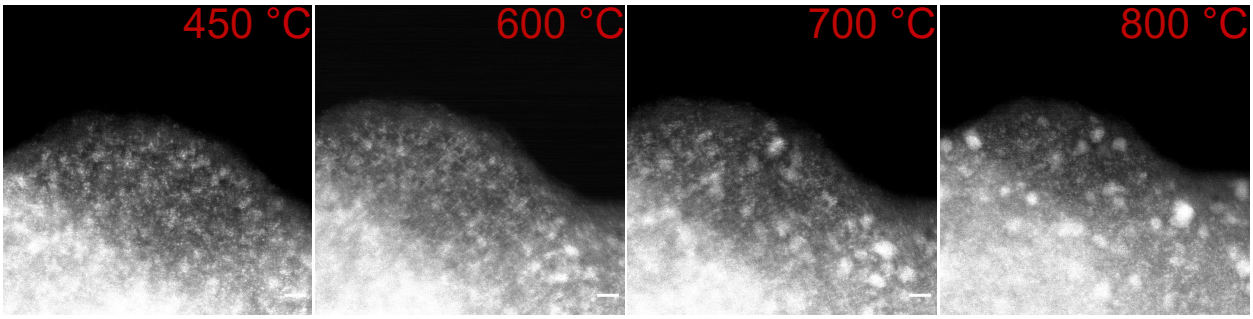


**Figure S10: a-d**, High-resolution in-situ heating STEM images of Pt sites at another edge area in the 10 wt% Pt-PANI sample at varied heating temperatures (450 °C, 600 °C, 700 °C, and 800 °C). The scale bar is 2 nm in **a-d**.

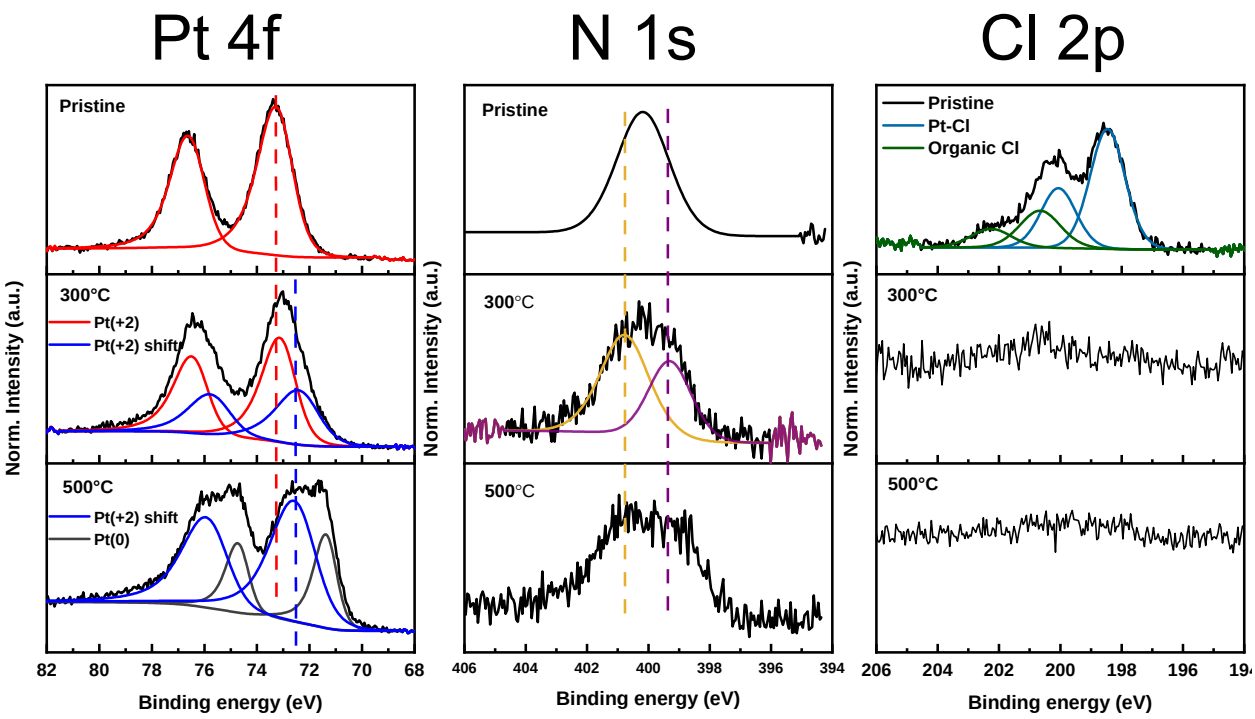


**Figure S11:** Ex-situ XPS spectra of the Pt 4f, N 1s and Cl 2p peaks of the 10 wt% Pt-PANI sample after heating at varied temperatures, showing the gradual reduction of Pt sites with increasing temperature

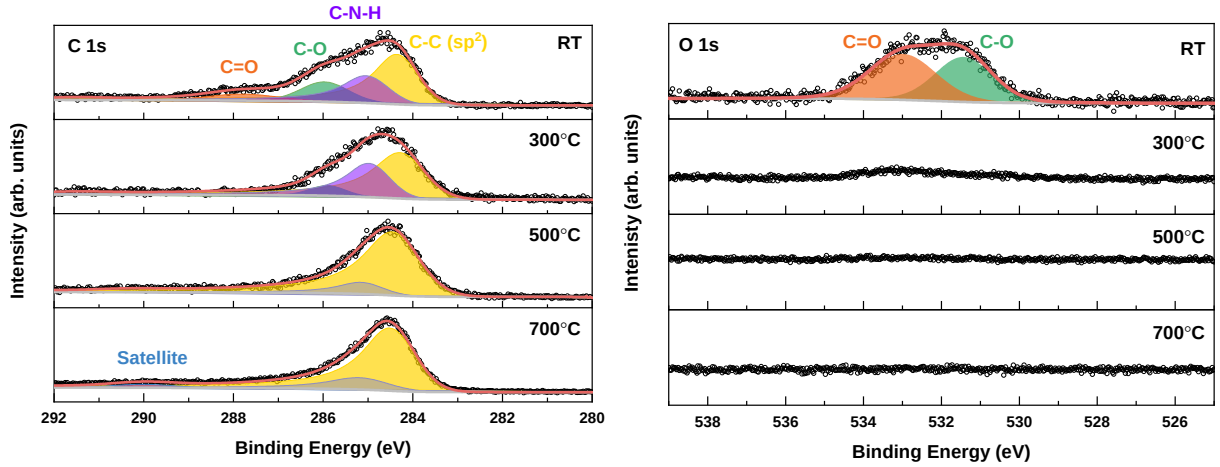


**Figure S12:** Temperature-dependent XPS spectra of the O 1s and C 1s peaks of the 1 wt% Pt-PANI sample at varying temperatures.

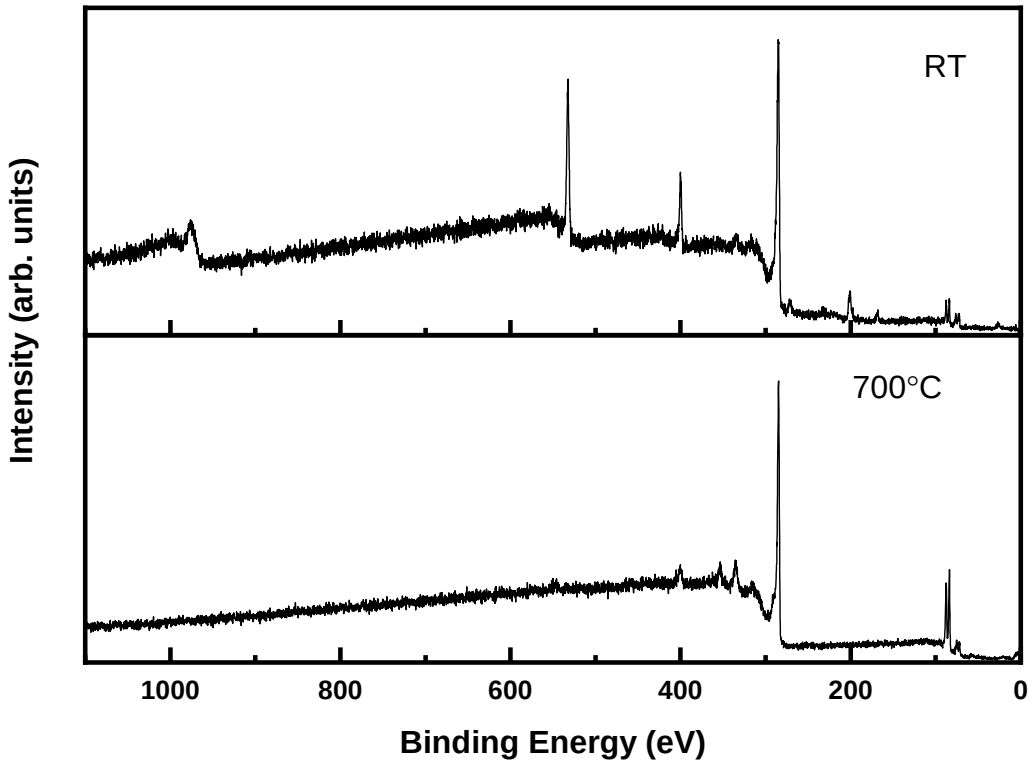


**Figure S13:** Temperature-dependent XPS spectra of the survey scans of the 1 wt% Pt-PANI sample at room temperature and 700 °C.

## Discussions on the protocol for HER testing

HER performance for Pt-based catalysts in acidic media is prone to underestimation due to limited mass transport of the hydrogen gas produced from the catalyst surface, which can prevent the catalytic active sites maintaining contact with the electrolyte. [14] This has been reported to significantly affect the assessment of the activity of the highly HER active commercial Pt on C catalysts. [15] To allow for a fair activity comparison of our Pt SSC with commercial Pt/C, we include the following measures in our electrochemical protocol to minimise the effect resulting from mass transport of $H_2$.

The working electrode (WE) is placed vertically inside the cell to allow the produced $H_2$ to dissipate easily from the surface. An external flow of $H_2$ is introduced to the electrolyte solution, perturbing the solution to help accelerate the mass transport while saturating it with $H_2$ to establish an accurate thermodynamic onset for the HER at the WE. A low sample loading (1 µg Pt $cm^{-2}$) is used to limit the amount of $H_2$ produced, reducing the probability of the $H_2$ generated covering the catalyst surface. This thin coating of the catalyst also ensures thorough wetting by the electrolyte. A reference $Hg/Hg_2SO_4$ electrode with a Luggin capillary geometry is used and placed around 5 mm from the WE to minimise ohmic loss, allowing accurate control of the applied potential bias. The Pt-mesh counter electrode with an electrochemically active surface area (ECSA) ten times that of the active materials on the WE is used to ensure the HER current is not limited by the counter reaction. The ECSA of Pt is determined by averaging the total charge for proton adsorption and desorption, which occur between ∼0.05 and 0.4 V in a cyclic voltammetry scan in argon, and dividing by the specific charge for polycrystalline Pt (210 µC $cm^{-2}{}_{Pt}$). Supplementary Fig. S14 shows the electrochemical setup we used.

To validate our electrochemical tests, we calculated the HER turnover frequency (TOF) of the commercial 20 %wt Pt/C and compared the value with the state-of-the-art mass-transfer optimised floating electrode [16] and $H_2$ pump techniques [17]. The TOF is defined as the rate of $H_2$ produced per active site and is calculated as

$$\mathrm{TOF} = \frac{n_{H_2}}{n_{site} \cdot \mathrm{time}} = \frac{i}{q_{HER/HOR} \cdot Q_{HUPD}} = \frac{i}{2 \cdot Q_{HUPD}} \tag{3}$$

where i is the measured HER/HOR current. $Q_{HUPD}$ denotes the integrated charge in the HUPD experiment. $q_{HER/HOR}$ is the number of charges transferred to evolve one $H_2$ molecule. Using our electrochemical setup, the 20 %wt Pt/C reached a TOF value of ∼100 at -0.1 V (Supplementary Fig. S15), which is approaching the same order of magnitude as the numbers from the $H_2$ pump (TOF ∼1000). Specific current density curves were plotted in Supplementary Fig. S15 by normalising the current by the ECSA of the 20 wt% commercial Pt/C sample, showing that an overpotential of 50 mV is required to reach a current density of 10 mA $cm^{-2}$.

We used the following protocol for the preparation of the working electrode: 20 wt% commercial Pt/C (1 mg) was mixed with ethanol (4 mL) and 5 wt% of Nafion (1 µL perfluorinated resin solution) and sonicated for at least 15 minutes. The mixture was subsequently stirred at a rate of 500 rpm for 2 hrs to make a well-dispersed catalyst ink. 20 µL of the catalysts were then dropped and coated on a glassy carbon electrode with an area of 1 $cm^2$ to achieve a catalyst loading of 1 µg Pt $cm^{-2}$ on each sample.

**Figure S14:** Photograph of the electrochemcial cell used.

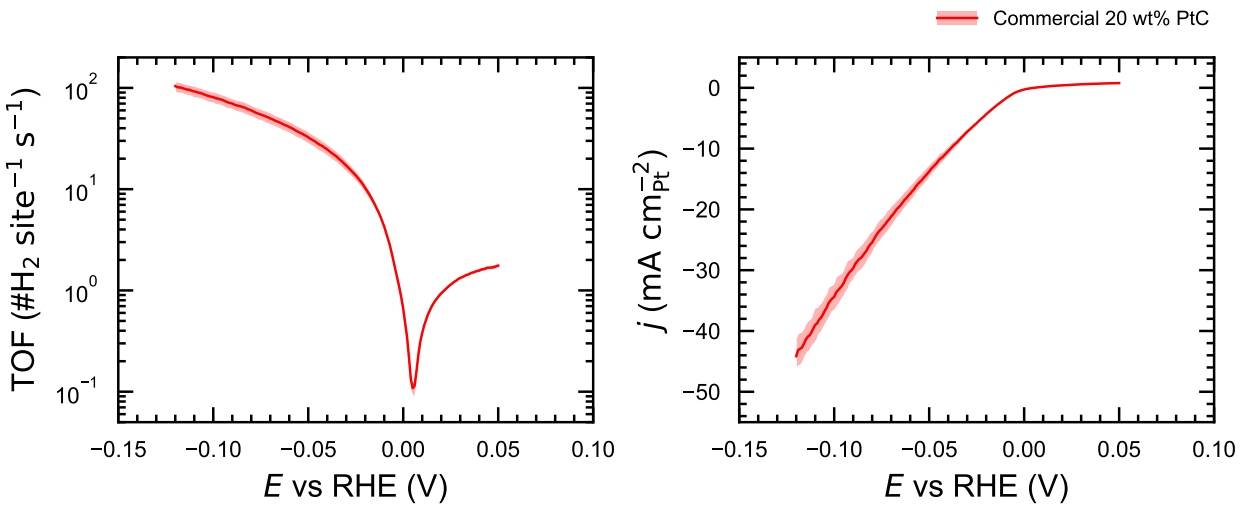


**Figure S15:** a) TOF polarisation curve and b) specific current density curve of the 20 wt% commercial Pt/C. The solid line is the average value from three independent measurements and the shaded area denotes the standard error.

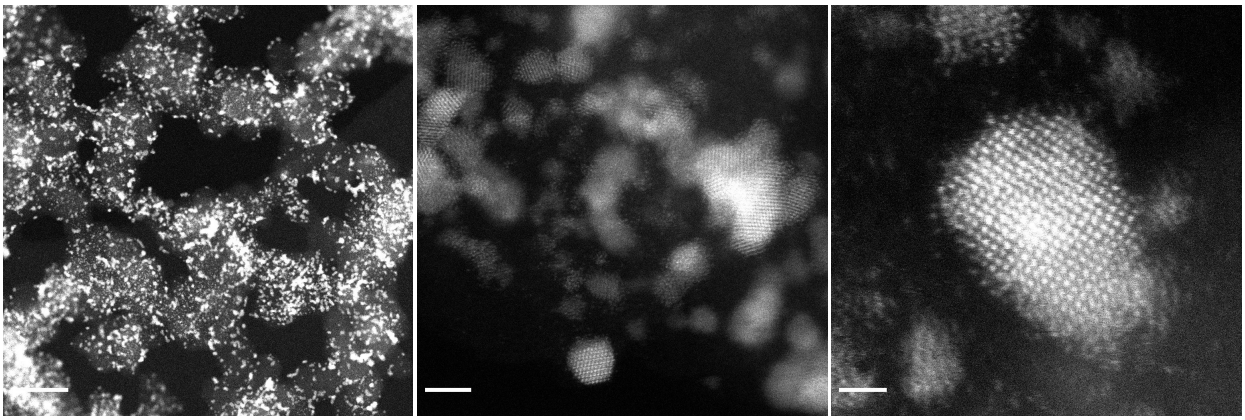

**Figure S16:** **a**-**c**, Low to high-resolution STEM images of the 20 wt% Pt/C showing well-dispersed Pt nanoparticles with an average size of around 3 nm on the carbon support. The scale bars are 50 nm in **a**, 3 nm in **b**, and 1 nm in **c**.

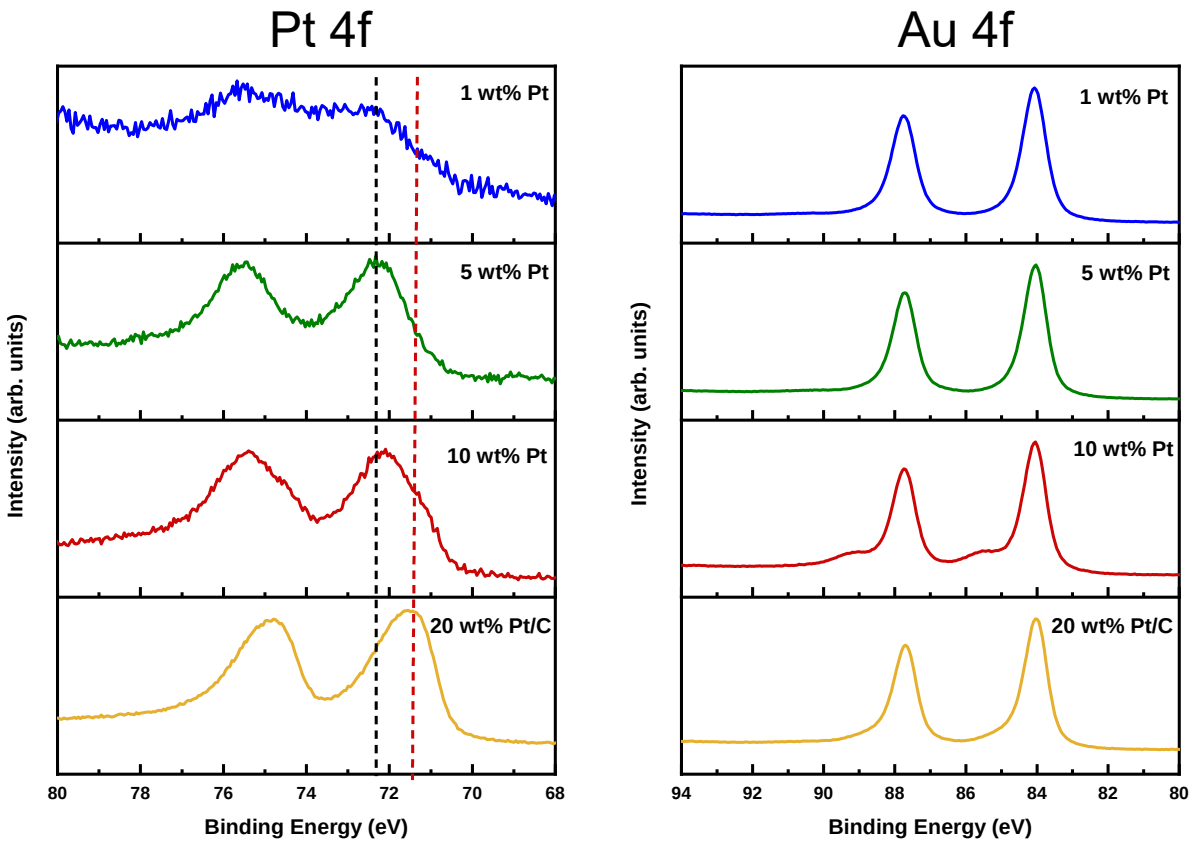


**Figure S17:** Ex-situ XPS data: Pt 4f and Au 4f (reference) spectra from the 1 wt% (blue), 5 wt% (green), 10 wt% (red) Pt-PANI samples after pyrolysis (the trapped Pt samples), and 20 wt% Pt/C (yellow).

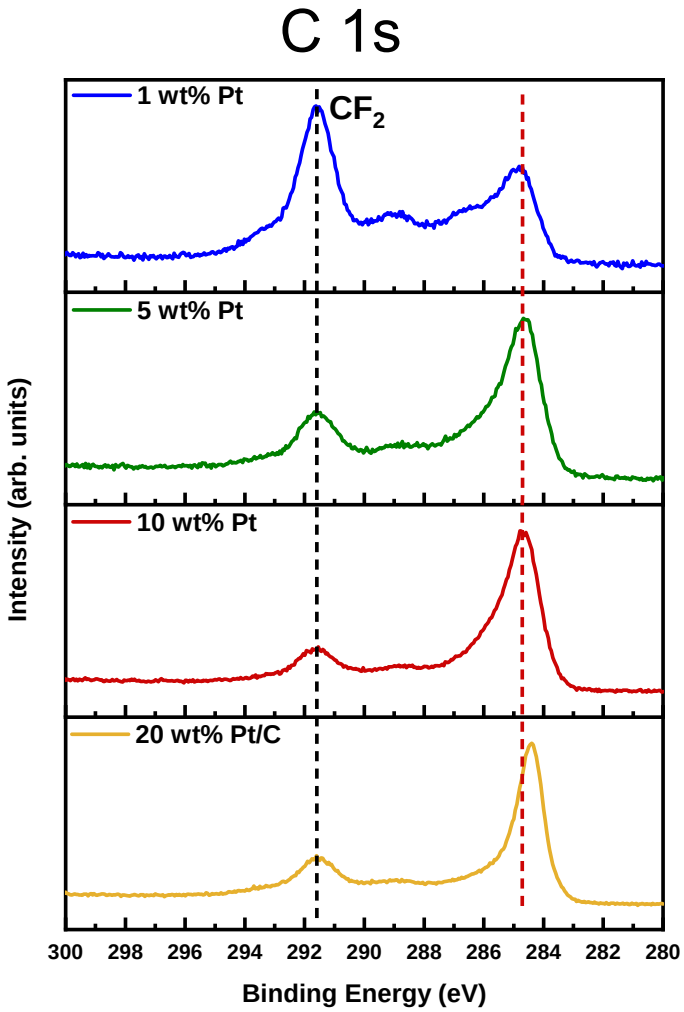


**Figure S18:** Ex-situ XPS spectra of C 1s from the 1 wt% (blue), 5 wt% (green), 10 wt% (red) Pt-PANI samples after pyrolysis (the trapped Pt samples) and 20 wt% Pt/C (yellow). The C 1s peaks of - $CF_2$ from the Nafion solution are all at 291.6 eV, which further confirms the shift in Pt 4f peaks of trapped Pt samples and 20 wt% Pt/C is reliable.

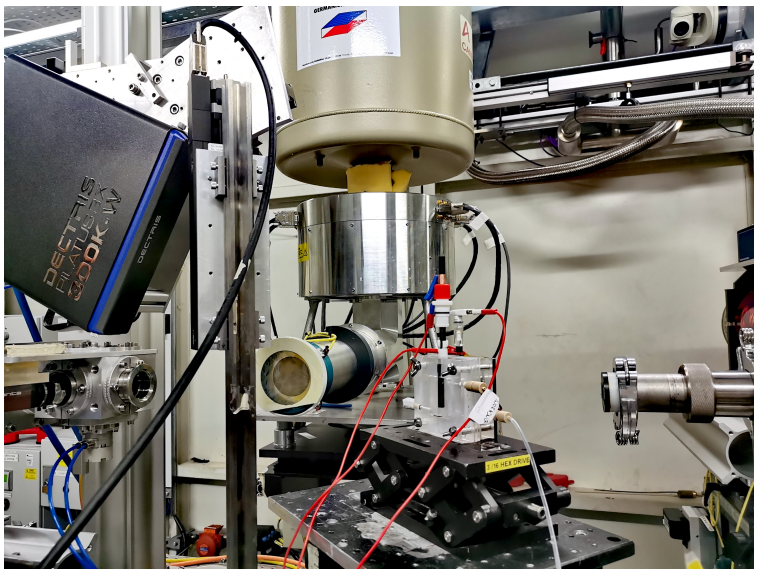


**Figure S19:** Photo of the operando XAS study at the Diamond beamline.

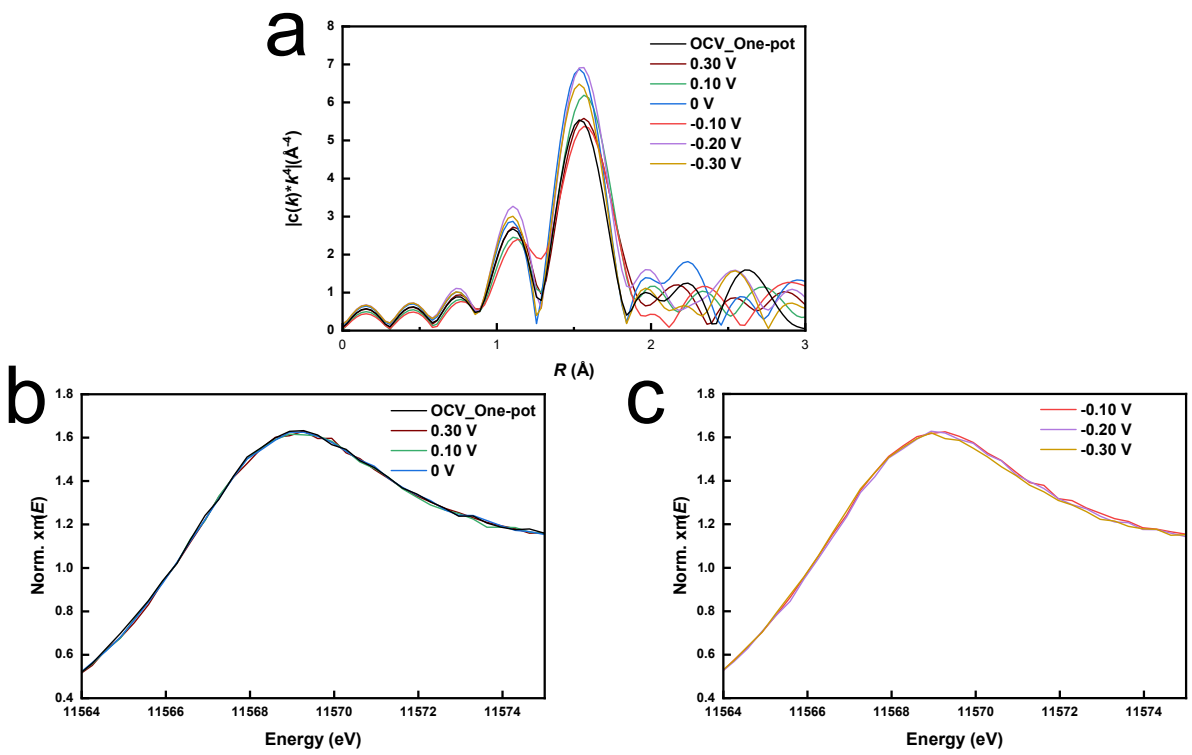


**Figure S20:** **a**, The FT-EXAFS spectra of Pt $L_3$-edge for the trapped Pt SSC at all applied potentials. **b**,**c**, XANES spectra of Pt-$L_3$ edge line for the trapped Pt SSC at applied potentials from OCV to 0 V (**b**) and -0.1 V to -0.3 V (**c**).

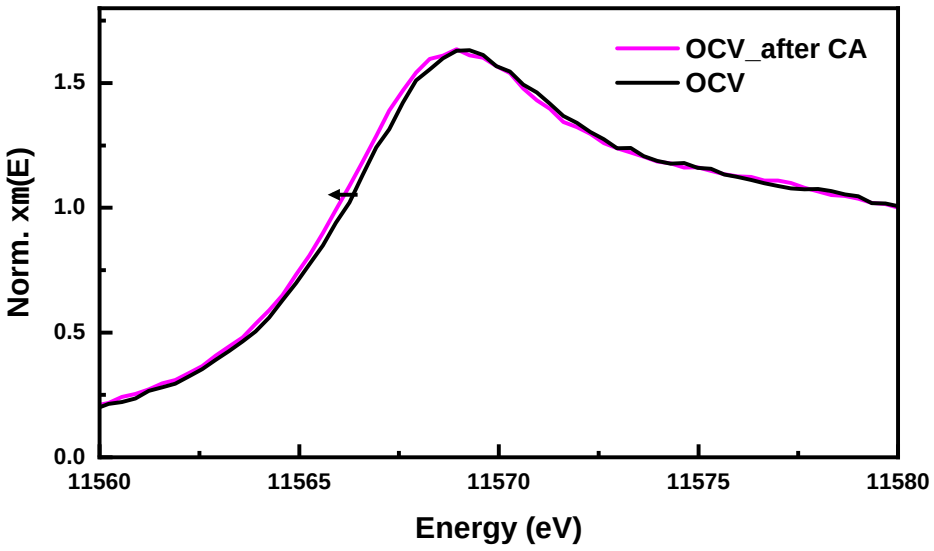


**Figure S21:** XANES spectra of Pt-$L_3$ edge line for the trapped Pt SSC at OCV before and after 2 hrs of CA testing.

**Table S2:** Curvefit parameters for Pt $L_3$-edge EXAFS data in operando experiment by DFT modelling of Pt-3N-C and Pt foil. $S_0{}^2$ is fixed as 0.80 and the coordination number of Pt-N is fixed as 3. The fitted data range in K space and R space is: 3 – 11 Å, 1.1 – 2.4 Å for all potentials. Debye-Waller factors were constrained as $\delta^2$(Pt-N)= $\delta^2$(Pt-N-C) to reduce the number of variables. The numbers in brackets are uncertainties for each fitting result.

| Sample | Path | CN | R(Å) enhanced | $\sigma(10^{-3}Å^2)$ | R-factor |
|---|---|---|---|---|---|
| Pt foil | Pt-Pt | 12 | -0.010 | 4.4(0.2) | 0.002 |
| As-synthesised | Pt-N | 3 | 0.019(0.010) | 4.5(0.7) | 0.017 |
| | Pt-N-C | 7.0(1.9) | 0.151(0.044) | | |
| OCV | Pt-N | 3 | 0.017(0.012) | 3.7(0.9) | 0.026 |
| | Pt-N-C | 9.4(2.8) | 0.140(0.048) | | |
| 0.10 V | Pt-N | 3 | 0.011(0.007) | 2.5(0.5) | 0.011 |
| | Pt-N-C | 7.1(1.7) | 0.131(0.036) | | |
| 0 V | Pt-N | 3 | 0.012(0.010) | 2.7(0.7) | 0.022 |
| | Pt-N-C | 7.1(2.2) | 0.156(0.048) | | |
| -0.10 V | Pt-N | 3 | 0.006(0.012) | 2.8(0.9) | 0.030 |
| | Pt-N-C | 8.3(2.8) | 0.136(0.053) | | |
| -0.30 V | Pt-N | 3 | 0.009(0.012) | 3.1(0.8) | 0.028 |
| | Pt-N-C | 7.4(2.6) | 0.130(0.054) | | |

# References


1. Kaiser, S. K. *et al.* Nanostructuring unlocks high performance of platinum single-atom catalysts for stable vinyl chloride production. *Nature Catalysis 2020 3:4* **3,** 376–385 (4 2020).
2. Ravel, B. & Newville, M. ATHENA, ARTEMIS, HEPHAESTUS: data analysis for X-ray absorption spectroscopy using IFEFFIT. *Journal of synchrotron radiation* **12,** 537–541 (2005).
3. Payne, M. C., Teter, M. P., Allan, D. C., Arias, T. & Joannopoulos, J. D. Iterative minimization techniques for ab initio total-energy calculations - molecular-dynamics and conjugate gradients. *Rev. Mod. Phys.* **64,** 1045–1097 (1992).
4. Clark, S. J. *et al.* First principles methods using CASTEP. *Z. Kristall.* **220,** 567–570 (2005).
5. Pfrommer, B. G., Cote, M., Louie, S. G. & Cohen, M. L. Relaxation of crystals with the quasi-Newton method. *J. Comput. Phys.* **131,** 233–240 (1997).
6. Perdew, J. P., Burke, K. & Ernzerhof, M. *Phys. Rev. Lett.* **77,** 3865 (1996).
7. McNellis, E., Meyer, J. & Reuter, K. Azobenzene at coinage metal surfaces: Role of dispersive van der Waals interactions. *Phys. Rev. B* **80,** 205414 (2009).
8. Ambrosetti, A., Reilly, A. M., DiStasio, R. A. & Tkatchenko, A. Long-range correlation energy calculated from coupled atomic response functions. *J. Chem. Phys.* **140,** 18A508 (2014).
9. Grimme, S., Antony, J., Ehrlich, S. & Krieg, H. A consistent and accurate ab initio parametrization of density functional dispersion correction (DFT-D) for the 94 elements H-Pu. *J. Chem. Phys.* **132,** 154104 (2010).
10. Nørskov, J. K. *et al.* Trends in the Exchange Current for Hydrogen Evolution. *Journal of The Electrochemical Society* **152,** J23 (3 2005).
11. Atkins, P. W. *Physical Chemistry, 6th ed.* (Oxford UniversityPress, Oxford, 1998).
12. Norskov, J. K. *et al.* Trends in the exchange current for hydrogen evolution. *Journal of The Electrochemical Society* **152,** J23 (2005).
13. Momma, K. & Izumi, F. VESTA 3 for three-dimensional visualization of crystal, volumetric and morphology data. *Journal of applied crystallography* **44,** 1272–1276 (2011).
14. Hansen, J. N. *et al.* Is There Anything Better than Pt for HER? *ACS Energy Letters* **6,** 1175–1180 (4 2021).
15. Zheng, J., Yan, Y. & Xu, B. Correcting the Hydrogen Diffusion Limitation in Rotating Disk Electrode Measurements of Hydrogen Evolution Reaction Kinetics. *Journal of The Electrochemical Society* **162,** F1470–F1481 (14 2015).
16. Zalitis, C. M., Kramer, D., Sharman, J., Wright, E. & Kucernak, A. R. Pt Nano-Particle Performance for PEFC Reactions at Low Catalyst Loading and High Reactant Mass Transport. *ECS Transactions* **58,** 39 (2013).
17. Durst, J., Simon, C., Hasché, F. & Gasteiger, H. A. Hydrogen Oxidation and Evolution Reaction Kinetics on Carbon Supported Pt, Ir, Rh, and Pd Electrocatalysts in Acidic Media. *Journal of The Electrochemical Society* **162,** F190–F203 (1 2015).